Dalton Transactions

PAPER

View Article Online
View Journal | View Issue

Cite this: *Dalton Trans.*, 2016, **45**, 4622

U(v) in metal uranates: a combined experimental and theoretical study of $MgUO_4$, $CrUO_4$, and $FeUO_4$†

Xiaofeng Guo,[a,b] Eitan Tiferet,[b,c] Liang Qi,[d,e] Jonathan M. Solomon,[d] Antonio Lanzirotti,[f] Matthew Newville,[f] Mark H. Engelhard,[g] Ravi K. Kukkadapu,[g] Di Wu,[b] Eugene S. Ilton,[h] Mark Asta,[d] Stephen R. Sutton,[f,i] Hongwu Xu[a] and Alexandra Navrotsky*[b]

Received 6th January 2016,
Accepted 2nd February 2016

DOI: 10.1039/c6dt00066e

www.rsc.org/dalton

Although pentavalent uranium can exist in aqueous solution, its presence in the solid state is uncommon. Metal monouranates, $MgUO_4$, $CrUO_4$ and $FeUO_4$ were synthesized for detailed structural and energetic investigations. Structural characteristics of these uranates used powder X-ray diffraction, synchrotron X-ray absorption spectroscopy, X-ray photoelectron spectroscopy, and ^{57}Fe-Mössbauer spectroscopy. Enthalpies of formation were measured by high temperature oxide melt solution calorimetry. Density functional theory (DFT) calculations provided both structural and energetic information. The measured structural and thermodynamic properties show good consistency with those predicted from DFT. The presence of U^{5+} has been solidly confirmed in $CrUO_4$ and $FeUO_4$, which are thermodynamically stable compounds, and the origin and stability of U^{5+} in the system was elaborated by DFT. The structural and thermodynamic behaviour of U^{5+} elucidated in this work is relevant to fundamental actinide redox chemistry and to applications in the nuclear industry and radioactive waste disposal.

Introduction

Metal monouranates, MUO_4, are of considerable interest due to their importance in actinide chemistry and nuclear technology.[1,2] They are also interesting from the crystal-chemical viewpoint, as their structures can incorporate uranium in the unusual pentavalent oxidation state, U(v). Uranium aqueous chemistry associated with geologic, environmental and technological applications is dominated by U^{6+} because of the greater solubility of its related uranyl (UO_2^{2+}) ion. This same ion dominates uranium chemistry in complex uranyl mineral phases, while in UO_2 and its associated compounds, the much less soluble U^{4+} species is present. The intermediate pentavalent state, U^{5+}, is far less common,[3–5] but can exist occasionally in aqueous solutions[6,7] and is expected to occur in monouranates, MUO_4, containing trivalent cations M^{3+}, while U^{6+} occurs with divalent M^{2+}. Thus these U(v) containing monouranates, with their simple stoichiometries, allow in-depth structural and stability investigations. In spite of the increasing attention to these compounds, only some of their structural characteristics have been studied,[2,8–21] and among those studies, few have used spectroscopic methods to probe local structures.[11,12,17,19,20] The oxidation state of U in $MgUO_4$ is generally regarded to be hexavalent,[11,21] yet those of U in $CrUO_4$ and $FeUO_4$ are less certain.[8,9] Moreover, there is limited thermodynamic data available for these simple monouranates,[2,10,13–16,18]

$MgUO_4$ was first synthesized by Haag *et al.*[22] using solid state methods. It has an orthorhombic structure with the space group *Imam*; the lattice parameters are a = 6.52 Å, b = 6.59 Å, and c = 6.92 Å.[23,24] X-ray photoelectron spectroscopy (XPS) was used to measure binding energies (BE) of the main

[a]*Earth and Environmental Sciences Division, Los Alamos National Laboratory, Los Alamos, NM 87545, USA. E-mail: anavrotsky@ucdavis.edu*
[b]*Peter A. Rock Thermochemistry Laboratory and Nanomaterials in the Environment, Agriculture and Technology Organized Research Unit, University of California, Davis, CA 95616, USA*
[c]*Nuclear Research Center – Negev Be'er-Sheva 84190, Israel Institution, Israel*
[d]*Department of Materials Science and Engineering, University of California, Berkeley, CA 94720, USA*
[e]*Department of Materials Science and Engineering, University of Michigan, MI 48109, USA*
[f]*Center for Advanced Radiation Sources, University of Chicago, Chicago, Illinois 60637, USA*
[g]*Environmental Molecular Sciences Laboratory, Pacific Northwest National Laboratory, Richland, WA 99354, USA*
[h]*Pacific Northwest National Laboratory, Richland, WA 99352, USA*
[i]*Department of Geophysical Sciences, University of Chicago, Chicago, Illinois 60637, USA*
†Electronic supplementary information (ESI) available. See DOI: 10.1039/c6dt00066e

U(4f) and satellite peaks, and to confirm the hexavalent state of U.[11]

$CrUO_4$ belongs to the $BiVO_4$ structure type. It was discovered in 1959 by Borchardt[25] from reaction of Cr_2O_3 and U_3O_8, and the pure phase was later synthesized by Felten *et al.*[8] Like other $BiVO_4$ type uranates, $CrUO_4$ crystallizes in the orthorhombic structure with a symmetry of *Pbcn*[26,27] and has lattice parameters a = 4.86 Å, b = 11.78 Å, and c = 5.04 Å.[8,25] It is argued that the exclusive presence of U^{6+} in this compound is unlikely due to the easy oxidation of Cr^{2+} to Cr^{3+}. Presence of U^{5+} or equal quantities of U^{4+} and U^{6+} may be more probable.[8] Structural analyses using techniques sensitive to local structure such as X-ray absorption near edge structure (XANES) and XPS can help potentially resolve this issue. $FeUO_4$, first studied in 1967 by Bacmann *et al.*[28] also possesses the $BiVO_4$ structure with lattice parameters a = 4.88 Å, b = 11.93 Å and c = 5.11 Å.[29] However, the oxidation states of U and Fe in $FeUO_4$ remain unclear, since U and Fe can adopt several possible combinations of oxidation states such as U^{6+}–Fe^{2+}, U^{4+}/U^{6+}–Fe^{3+}, U^{5+}–Fe^{3+}, and any mixture of these three configurations. It has been suggested that U is pentavalent in this compound, based on a magnetic measurement where a small moment on U was observed.[29]

To obtain a better understanding of the local structure of U in these compounds, we employed four complementary spectroscopic techniques: XANES and XPS that provide direct evidence of the oxidation state of U, extended X-ray absorption fine structure (EXAFS) that gives the associated bonding information, and Mössbauer spectroscopy for determination of the Fe oxidation state. The results of these studies are complimented by density functional theory (DFT) calculations of electronic structures based on the generalized-gradient approximation (GGA) with Hubbard-*U* corrections (see Methods). The calculations are used to investigate the relationships between the structural features associated with U^{5+}/U^{6+} cations, the electronic structure and thermodynamic stability.[30–35] The existence of U^{5+} in $CrUO_4$ or $FeUO_4$ has been confirmed to facilitate the formation and stabilize the structure of both uranates. The predictions of thermodynamic stability are compared to direct calorimetry measurements of the formation enthalpies performed in this work.

In addition, the present DFT and calorimetry results for the formation energies of for $MgUO_4$, $FeUO_4$ and $CrUO_4$ are compared with previously published experimental results,[2,13–15,18] for MUO_4 with M = Ca^{2+}, Sr^{2+} and Ba^{2+}. $CaUO_4$ has a rhombohedral structure with space group $R\bar{3}m$; the lattice parameters are a = 6.25 Å and α = 36.0°.[36] $SrUO_4$ and $BaUO_4$ have an orthorhombic structure with space group *Pbcm*; the lattice parameters are, respectively, a = 5.49 Å, b = 7.98 Å, c = 8.13 Å,[37] and a = 5.76 Å, b = 8.14 Å, c = 8.23 Å.[38] Among the uranate compounds with divalent metals, the formation enthalpy is found to become increasingly negative as the ionic radius of M^{2+} increases. From an analysis of measured bond lengths and DFT calculations, these results are shown to be correlated with trends in Lewis acid/base chemistry across the compounds.

Results

Structure and composition

The phase purity, homogeneity and chemical composition of each synthetic monouranate sample were examined by electron probe microanalysis (EPMA), and the results are shown in Table S1 in ESI.† The measured contents of Mg, Cr, Fe, and U are stoichiometric within analytical uncertainties. The obtained chemical formulae are: $Mg_{0.98}U_{1.02}O_4$, $Cr_{0.98}U_{1.02}O_4$, and $Fe_{1.00}U_{1.00}O_4$.

All the samples were characterized by XRD (Fig. 1) for phase identification and lattice parameter determination. Again, no impurities were detected. The refined lattice constants are listed in Table 1 and are generally consistent with those reported in the literature,[8,23–25,29] A comparison of the measurements and the DFT calculated lattice parameters obtained in this work is also given in Table 1, where it is shown that computed lattice parameters (volume) overestimate the measured values by a few percent (4.5–5.9%); such a level of agreement is similar to that found in calculations in the current work for UO_2, and UO_3, and in previous calculations employing similar DFT + *U* methods for U_3O_8.[39]

The structure of $MgUO_4$ is orthorhombic with space group *Imam*.[23] Each Mg or U cation is located in an octahedron surrounded by six O^{2-} anions, and there are two types of O^{2-} anions with symmetry-inequivalent nearest neighbors of Mg and U cations. [MgO_6] or [UO_6] octahedra form chains parallel to the c axis *via* edge sharing, and each [MgO_6] octahedral chain is linked to four [UO_6] chains and *vice versa* through corner sharing (Fig. 2). The obtained unit-cell parameters of $MgUO_4$ are a = 6.5230(1) Å, b = 6.5956(1) Å, and c = 6.9232(1) Å. $CrUO_4$ and $FeUO_4$ have the same structure, which is orthorhombic with the space group *Pbcn*.[26–28] Like Mg and U in the $MgUO_4$ structure, each Cr, Fe or U cation is coordinated to six O^{2-} anions (there are two types of crystallographically distinct O^{2-} anions), forming [CrO_6], [FeO_6] or [UO_6] octahedra

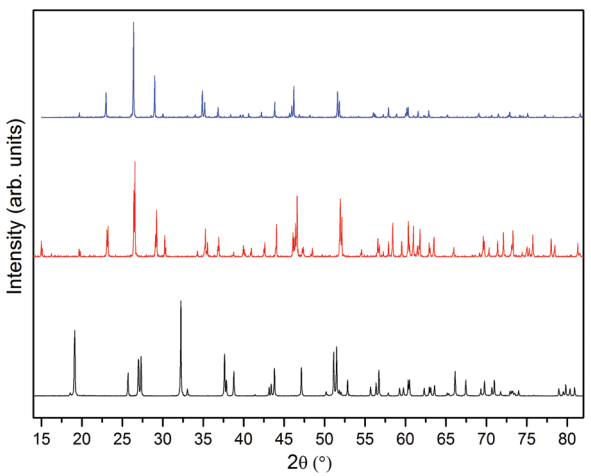

Fig. 1 Powder XRD patterns of $MgUO_4$ (black), $CrUO_4$ (red), and $FeUO_4$ (blue).

Table 1 Unit cell parameters of monouranates refined from XRD and calculated by DFT

		a (Å)	b (Å)	c (Å)	Volume (Å^3)	Difference[a] (%)
$MgUO_4$	XRD	6.5230(1)	6.5956(1)	6.9232(1)	297.85(1)	
	DFT	6.595	6.705	7.038	311.22	4.5
$CrUO_4$	XRD	4.87497(9)	11.8002(2)	5.06187(9)	291.19(1)	
	DFT	4.937	12.054	5.180	308.28	5.9
$FeUO_4$	XRD	4.8858(1)	11.9288(2)	5.1072(1)	297.65(1)	
	DFT	4.975	12.109	5.173	311.65	4.7

[a] Differences are obtained from comparison the volume values between the XRD and DFT values.

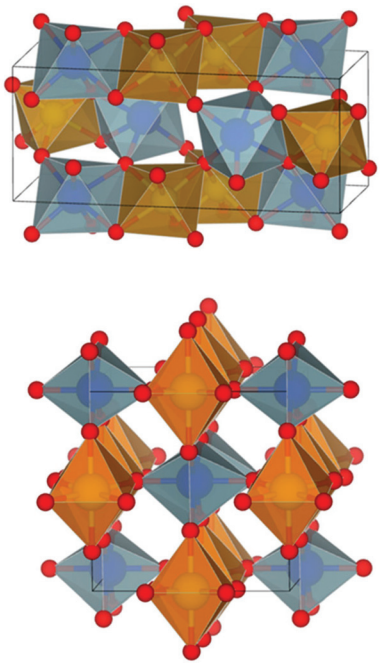

Fig. 2 Crystal structures of $MgUO_4$ (top) and $CrUO_4$ and $FeUO_4$ (bottom). Note that $CrUO_4$ and $FeUO_4$ are isostructural. Blue – [UO_6]; Orange – [MO_6], where M is the non-uranium metal cation.

Table 2 Interatomic distances (Å) in monouranates obtained from XRD and U EXAFS, and calculated by DFT

		XRD[a] (Å)	EXAFS (Å)	DFT (Å)
$MgUO_4$	U–O	1.9243	1.9347	1.96
		2.1599	2.1349	2.20
		2.2052	2.2146	2.20
	Mg–O	1.9804		2.04
		2.1920		2.21
$CrUO_4$	U–O	2.0610	2.0453	2.15
		2.1552	2.1499	2.20
		2.2189	2.1914	2.26
	Cr–O	2.0234		2.01
		2.0425		2.01
		2.0525		2.04
$FeUO_4$	U–O	2.0465	2.0769	2.15
		2.1820	2.1510	2.20
		2.2154	2.2163	2.26
	Fe–O	1.9913		2.02
		2.0515		2.03
		2.0901		2.06

[a] Calculated based on our determined unit-cell parameters and the atomic coordinates reported in literature (ref. 22, 26 and 27).

(although [MgO_6] has two different Mg–O lengths whereas all other octahedra have three Cr/Fe/U–O lengths; Table 2). Neighboring [CrO_6] or [FeO_6] and [UO_6] octahedra are connected *via* corner or edge sharing to form a three-dimensional framework (Fig. 2). The refined unit cell parameters of $CrUO_4$ are a = 4.87497(9) Å, b = 11.8002(2) Å, and c = 5.06187(9) Å. For $FeUO_4$, the refined unit cell parameters from XRD are a = 4.8858(1) Å, b = 11.9288(2) Å, and c = 5.1072(1) Å. Table 2 lists the U–O, Mg–O, Cr–O and Fe–O bond lengths obtained from XRD, EXAFS and DFT. With the exception of some of the U–O bonds in the $CrUO_4$ and $FeUO_4$ compounds, where the discrepancy is as large as 5%, the calculated and measured bond lengths in Table 2 are seen to agree to within 5%. Note that the U–O bond lengths of $CrUO_4$ and $FeUO_4$ are both larger than that of $MgUO_4$, which is possibly due to presence of U^{5+}, or to a mixture of U^{4+} and U^{6+}. Because the average bond length corresponding to a mixture of U^{4+} and U^{6+} is similar to that for U^{5+}, and Pauling's rules are not violated in either case, crystal chemistry solely cannot constrain the oxidation state of uranium in this structure.

U L_{III} XANES spectra were collected on all three uranate samples (Fig. 3). The U L_{III} spectrum of $MgUO_4$ shows an absorption edge energy (E_0) of 17 170.4 eV. This value is consistent with the U^{6+} oxidation state.[5] The $CrUO_4$ and $FeUO_4$

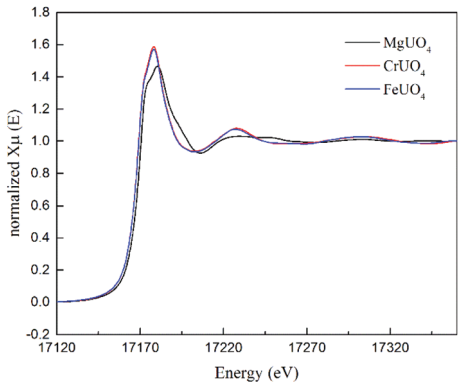

Fig. 3 U L_{III} XANES spectra of the three monouranates.

spectra show lower E_0 values of 17 169.5 and 17 169.7 eV, respectively. The reported difference between absorption edges for U(IV) and U(VI) is on the order of 3.0 to 4.0 eV.[40–42] The U(V) absorption edge is intermediate between those of U(IV) and U(VI), and the E_0 shifts from U(V) to U(VI) are in the range of 0.8–2.0 eV.[19,40–42] However, the absorption edge energy may not be a sole function of oxidation state and can be affected by such factors as the type of species, its chemical environment and bonding characteristics. For instance, E_0 values for compounds possessing highly covalent, π-ponded metal ligand multiple bonds often differ significantly from those for compounds with the same formal valence but exhibiting solely α-bound ligands.[42]

For the U L_{III} absorption edges of the three uranates, since the E_0 values of $CrUO_4$ and $FeUO_4$ are 0.9 and 0.7 eV, respectively, lower than that of $MgU(VI)O_4$, the U in $CrUO_4$ and $FeUO_4$ probably has an oxidation state of U(V). Moreover, EXAFS fitting of the spectra yielded the coordination number of the first shell from the central U: $N = 6.0 \pm 0.6$, $\sigma^2 = 0.003 \pm 0.002$ for $MgUO_4$, $N = 5.9 \pm 0.3$, $\sigma^2 = 0.001 \pm 0.001$ for $CrUO_4$ and $N = 6.0 \pm 0.4$, $\sigma^2 = 0.001 \pm 0.001$ for $FeUO_4$, thereby confirming the octahedral coordination of U despite its different valences in the three compounds.

XPS was performed to confirm the determined oxidation states of U. The obtained spectra are shown in Fig. 4. CasaXPS software V2.3.16 was used to fit the U $4f_{7/2}$ line after Shirley background subtraction. U(V) was fit using one peak component with a full-width-at-half-maximum (FWHM) of 1.15 eV, and U(VI) was fit with two peak components with the same FWHM as for U(V). Each line was fit using a mixture of 60% Gaussian and 40% Lorentzian including an asymmetric peak function described in CasaXPS as A(0.3, 0.2) GL(40) to model the data envelope. In the spectrum of $MgUO_4$, the $U4f_{7/2}$ line has only one BE for the U^{6+} peak at 381.3 eV. Spectra of $CrUO_4$ and $FeUO_4$ have their main $U4f_{7/2}$ energy peaks located at 380.2 eV and 380.4 eV, respectively, indicative of U^{5+}. They also contain minor peaks in the range of 381.4–382.3 eV, representing U(VI) binding energies (BEs), and U^{5+} satellite structures at ~388.7 eV and ~399.4 eV. Gaussian functions were used to model $U4f_{7/2}$ (Shirley background) for quantification of U oxidation states (Fig. 4, Table S2 in ESI†). The obtained results show that the U^{5+}/U ratios of $CrUO_4$ and $FeUO_4$ are 50.7% and 66.4%, respectively. However, because of possible surface oxidation and since XPS is a near-surface technique, these values do not represent the U valence information for the bulk samples, as revealed by U L_{III} XANES. In fact, XPS showed that Cr and Fe in $CrUO_4$ and $FeUO_4$ are both trivalent, implying the occurrence of U^{5+} or possible mixture of U^{4+} and U^{6+} in the structure to achieve charge neutrality.

Transmission ^{57}Fe Mössbauer spectroscopy, which is specific to the ^{57}Fe isotope (a stable isotope of Fe with a natural abundance of 2.2%) and is a bulk technique, was employed to characterize the oxidation state of Fe in $FeUO_4$. Room temperature (RT), 77 K and 35 K (below the Curie temperature, 42 K (ref. 29)), data were collected (Fig. 5). The center shift (CS) of the intense doublet in the RT spectrum, 0.38 mm s^{-1}

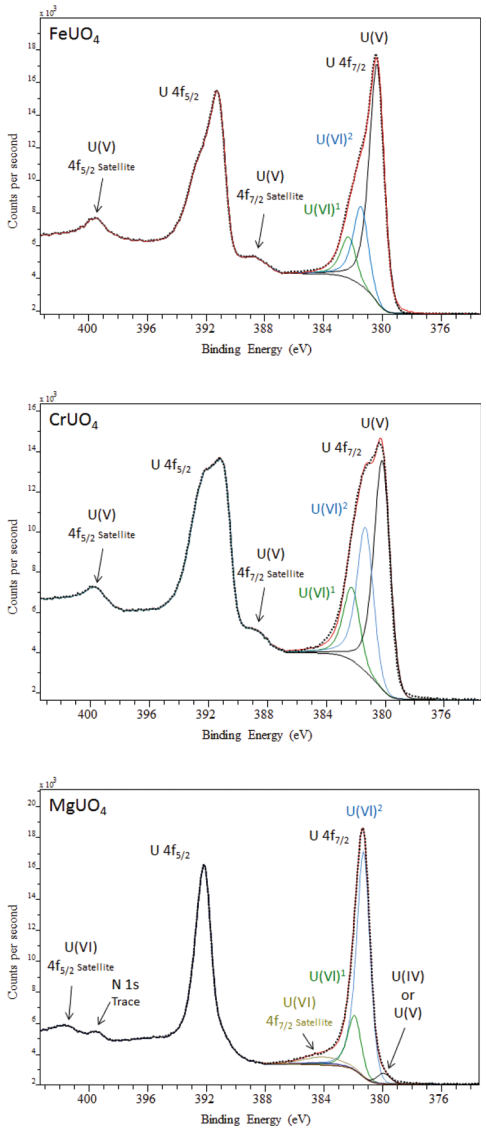

Fig. 4 XPS spectra of the U 4f region for $MgUO_4$ (bottom), $CrUO_4$ (middle), and $FeUO_4$ (top).

with respect to α-Fe standard, suggests it to be high spin Fe(III).[43] Its quadrupole splitting (QS), 0.21 mm s^{-1}, is also in agreement with a non-cubic local environment of Fe, as in the $FeUO_4$ structure. Bacmann *et al.*[29] reported a similar CS value for Fe in $FeUO_4$. The transformation of the RT doublet to sextet at 35 K spectrum is predominantly due to magnetic ordering of Fe in $FeUO_4$ (CS = 0.55 mm s^{-1}; quadrupole shift parameter (e) is −0.09 mm s^{-1}; and magnetic hyperfine field (H) is 42.6 Tesla). The minor sextet in the 35 K spectrum is due to the existence of an impurity, probably nano hematite. Furthermore, the combination of room temperature CS and QS values unambiguously suggests that the local geometry is different from that in well-known high temperature Fe(III)–oxide phases that may precipitate under these conditions; these oxides display QS of 0.5–0.7 mm s^{-1} at room temperature.[43] Given this and absence of sextet features at 77 K and

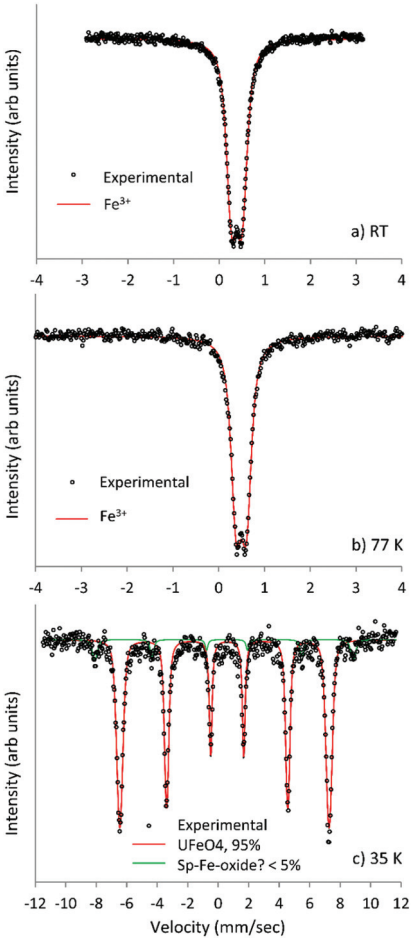

Fig. 5 Mössbauer spectra of $FeUO_4$ measured at RT (a), 77 K (b), and 35 K (c). Modeled spectra was shown in (c) for showing possible Fe oxide impurity.

the observed 35 K spectral parameters that are significantly different than typical Fe–oxides, and similarity of the spectral parameters to those in Bacmann *et al.*[29] study, it is clear that Fe(III) exists a non-cubic environment in $FeUO_4$.

Enthalpies of formation

$MgUO_4$. The calorimetric measurement on $MgUO_4$ was conducted using $3Na_2O{\cdot}4MoO_3$ molten solvent at 702 °C. We then derived the enthalpy of formation of $MgUO_4$ ($\Delta H_{f,ox}(MgUO_4)$ = −33.8 ± 1.7 kJ mol^{-1}, Table 3) from its binary oxides (MgO, γ-UO_3) based on the following reaction (1) through the thermochemical cycles and known drop solution data of the oxides shown in Table S3 in ESI.†

$$\gamma\text{-}UO_{3(s,25°C)} + MgO_{(s,25°C)} \rightarrow MgUO_{4(s,25°C)} \quad (1)$$

The DFT derived enthalpy of formation is −18.1 kJ mol^{-1}, which is less exothermic than the experimental value. The discrepancy may be due to errors from the GGA + *U* description of the bonding in the uranates containing divalent metals, as discussed below. The standard enthalpy of formation from the elements (ΔH_f°, Table 3) of $MgUO_4$, calculated by combining

Table 3 Enthalpies of formation of MUO_4 urinates from binary oxides and elements

Uranates	Binary oxides[a]	$\Delta H_{f,ox}$ (kJ mol^{-1})	ΔH_f° (kJ mol^{-1})
$BaUO_4$	BaO, γ-UO_3	−216.3 ± 3.0[2]	−1988.2 ± 2.0[2]
		−221.9 ± 4.0[14]	−1993.8 ± 3.3[14]
$SrUO_4$	SrO, γ-UO_3	−170.0 ± 1.9[13,15]	−1985.1 ± 1.4[15]
$CaUO_4$	CaO, γ-UO_3	−142.8 ± 2.4[2]	−2001.7 ± 2.1[2]
		−143.1 ± 3.0[18]	−2002.0 ± 3.2[18]
		−101.4[14]	−1960.3[14]
$MgUO_4$	MgO, γ-UO_3	−33.8 ± 1.7	−1859.2 ± 1.9
		−31.6 ± 1.7[10,13]	−1857.0 ± 1.3[10]
$CrUO_4$	Cr_2O_3, γ-UO_3, UO_2	−33.4 ± 1.3	−1824.6 ± 4.5
$FeUO_4$	Fe_2O_3, γ-UO_3, UO_2	−32.2 ± 2.8	−1599.7 ± 3.0
		−21.3 ± 1.7[13,16,44]	−1588.7 ± 1.2[16]

[a] Binary oxides are the reference phases for deriving $\Delta H_{f,ox}$ values of uranates.

$\Delta H_{f,ox}(MgUO_4)$ with reference data,[13,45] is −1859.2 ± 1.9 kJ mol^{-1}. This value agrees well with a previous measured ΔH_f°, −1857.0 ± 1.3 kJ mol^{-1},[10] obtained using a different solution calorimetric approach, where strong HNO_3 or a dilute aqueous mixture of HF + HNO_3 was used as the solvent.[9]

$CrUO_4$. The calorimetric measurements on $CrUO_4$ and its related binary oxides Cr_2O_3, UO_2 and γ-UO_3 were conducted in molten $3Na_2O{\cdot}4MoO_3$ solvent at 802 °C. Thorough dissolution of samples occurred at 802 °C but not at 702 °C due to slow dissolution. The drop solution experiment on uranium oxides was carried on $UO_{2.06}$ and γ-UO_3, and their ΔH_{ds} were measured to be −116.80 ± 0.80 kJ mol^{-1} and 26.11 ± 1.47 kJ mol^{-1}, respectively. $\Delta H_{ds}(UO_{2.06})$ was then corrected for the presence of additional 0.06 mol of oxygen atoms per formula unit of U^{4+} (reaction (9) in Table S4 in ESI†). The corrected ΔH_{ds} of UO_2 was −128.64 ± 1.61 kJ mol^{-1}. To confirm the accuracy of this value, oxidation enthalpy of UO_2 to γ-UO_3 at room temperature derived from ΔH_{ds} values in molten $3Na_2O{\cdot}4MoO_3$ solvent at 802 °C was compared with reference data.[13] Applying the oxidation reaction (10) in Table S4 in ESI,† the calculated enthalpy of oxidation based on our calorimetric data is −142.1 ± 2.2 kJ mol^{-1}, and that calculated from reference data is −138.8 ± 1.3 kJ mol^{-1}.[13] The difference is about 2%, which is on the order of experimental error. Therefore, we conclude that ΔH_{ds} of UO_2 and γ-UO_3 obtained from this experiment are accurate and the final state of U in $3Na_2O{\cdot}4MoO_3$ molten solvent is U^{6+}, regardless of the oxidation state of U (4+ or 6+) in the starting materials. $\Delta H_{ds}(Cr_2O_3)$ and $\Delta H_{ds}(CrUO_4)$, were directly obtained from the calorimetric measurement. The formation reaction of $CrUO_4$ from its binary oxides at room temperature is:

$$1/2\gamma\text{-}UO_{3(s,25°C)} + 1/2UO_{2(s,25°C)} + 1/2Cr_2O_{3(s,25°C)} \rightarrow CrUO_{4(s,25°C)} \quad (2)$$

$\Delta H_{f,ox}(CrUO_4)$ was calculated based on reaction (2) from the measured drop solution data through the thermochemical cycles in Table S4 in ESI.† The obtained $\Delta H_{f,ox}(CrUO_4)$ is −33.4 ± 1.3 kJ mol^{-1}. The DFT derived value the corresponding

enthalpy of reaction is −29.9 kJ mol^{-1}, 10% less exothermic than the measured value. Finally, the standard enthalpy of formation from the elements, ΔH_f° ($CrUO_4$), is determined from experimental measurements to be −1824.6 ± 4.5 kJ mol^{-1} (Table 3).

$FeUO_4$. Since $FeUO_4$ dissolves incompletely in molten $3Na_2O{\cdot}4MoO_3$ solvent, which generates small heat effects, molten lead borate ($2PbO{\cdot}B_2O_3$) solvent at 802 °C was used instead for its drop-solution calorimetric experiment. In a previous study,[46] we measured the ΔH_{ds} of UO_2 and γ-UO_3 in $2PbO{\cdot}B_2O_3$ at 802 °C, which are −125.21 ± 3.41 kJ mol^{-1} and 26.67 ± 4.02 kJ mol^{-1}, respectively. Their accuracy can be validated against the oxidation enthalpy at room temperature. The enthalpy of oxidation from UO_2 to γ-UO_3 calculated from these two ΔH_{ds} values is −139.2 ± 5.3 kJ mol^{-1}, which is 0.3% different from the value calculated from reference data.[13] Complete dissolution of $FeUO_4$ was confirmed by a furnace test, and the heat effect was large enough for accurate measurements. The obtained ΔH_{ds} and thermochemical cycles in Table S5 in ESI,† were used to calculate the enthalpies of formation of $FeUO_4$ with respect to two different binary oxide assemblages, (UO_2, γ-UO_3, Fe_2O_3) and (U_3O_8, Fe_3O_4). The obtained $\Delta H_{f,ox}$ values corresponding to reactions (3) and (4) are −32.2 ± 2.8 and −34.6 ± 4.2 kJ mol^{-1}, respectively.

$$1/2\gamma\text{-}UO_{3(s,25^\circ C)} + 1/2UO_{2(s,25^\circ C)} + 1/2Fe_2O_{3(s,25^\circ C)} \rightarrow FeUO_{4(s,25^\circ C)}. \quad (3)$$

$$1/3U_3O_{8(s,25^\circ C)} + 1/3Fe_3O_{4(s,25^\circ C)} \rightarrow FeUO_{4(s,25^\circ C)} \quad (4)$$

The enthalpy of formation calculated by DFT based on reaction (3) is −27.0 kJ mol^{-1}. This value shows a comparable level of agreement with experiment as reported above for $CrUO_4$, and is 16% less exothermic than the calorimetry value. It is also noted that our measured value of $\Delta H_{f,ox}$ for reaction (4), −34.6 ± 4.2 kJ mol^{-1}, is more exothermic than a recently reported $\Delta H_{f,ox}$, −25.2 ± 0.6 kJ mol^{-1}.[16] Although the latter calorimetric experiment also used $2PbO{\cdot}B_2O_3$ as the solvent, it was at 715 °C in air and the $FeUO_4$ sample used contains U_3O_8 as an impurity phase. The calculated standard enthalpy of formation of $FeUO_4$ from the elements based on our own $\Delta H_{f,ox}$ value is −1599.7 ± 3.0 kJ mol^{-1}.

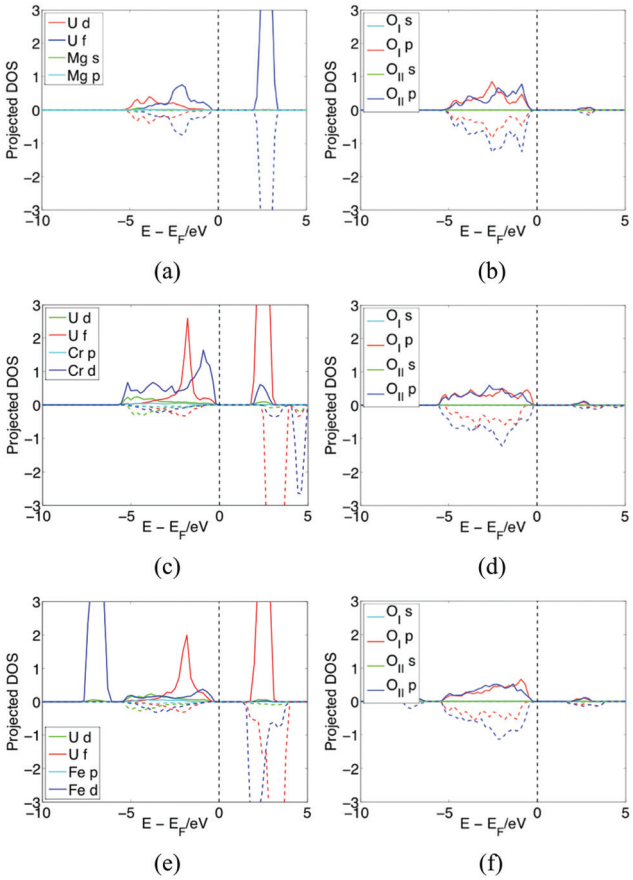

Fig. 6 Projected electronic densities of states (pDOS) calculated by DFT + *U* methods are plotted for: $MgUO_4$ for (a) U and Mg states and (b) the states associated with the two symmetry-distinct O anions; $CrUO_4$ for (c) U and Cr states and (d) the states associated with the two symmetry distinct O anions; pDOS of $FeUO_4$ for (e) U and Fe states and (f) the states associated with the two symmetry distinct of O anions. In each of the plots up-spin and down-spin states are plotted with positive and negative values, respectively.

Discussion

Structure of uranates

The oxidation state of U in $MgUO_4$ was confirmed by both XPS and XANES to be hexavalent. These results are in agreement with the GGA + *U* calculations shown in Fig. 6a and b, which plot the projected density of states (pDOS) for each type of symmetry-inequivalent ion in $MgUO_4$. For the U cation, the results show partial f and d state character below the Fermi level, which are strongly hybridized with the p states of the O^{2-} anions (Fig. 6b). This strong hybridization is consistent with the covalent character of the U(VI)–O uranyl bond. The projected total magnetic moment of the U cation is close to zero, as would be expected for a U cation with nominal U^{6+} oxidation state. A similar plot for the Mg cation is also shown in Fig. 6a, which has negligible pDOS below the Fermi level, consistent with a Mg^{2+} oxidation state.

Fig. 6 also plots the calculated electronic density of states for $CrUO_4$ and $FeUO_4$; again the pDOS for each symmetry-inequivalent ion are plotted. In sharp contrast to the results for $MgUO_4$, there is a large peak with dominant U f state character below the Fermi level for both $CrUO_4$ and $FeUO_4$. The peak is only for "up-spin" states, and corresponds to one unpaired f valence electron, as expected in a U^{5+} cation. In addition, large peaks with dominant transition-metal d state character can be observed on the Cr and Fe cations, which correspond to three unpaired spin-up d valence electrons in Cr^{3+} and five in Fe^{3+}. The calculated local magnetic moment of approximately 5μ_B for Fe is consistent with the Mössbauer spectroscopy finding of Fe being in a high-spin Fe^{3+} oxidation state (see above). Overall, the results of the DFT + *U* calculations are consistent with a picture corresponding to the presence of U^{5+},

Fe^{3+} and Cr^{3+} oxidation states in $FeUO_4$ and $CrUO_4$, in agreement with the XANES, XPS, and Mössbauer results.

Stability of U^{5+} in $FeUO_4$

In $CrUO_4$ and $FeUO_4$, the U^{5+} cation has a magnetic moment of $\pm 1\mu_B$ originating from one unpaired 5f occupied electron state (Fig. 6). Among many possible combinations of magnetic moment configurations in a primitive cell of $CrUO_4$ or $FeUO_4$, the ferromagnetic state was chosen to calculate the enthalpies of formation of $CrUO_4$ and $FeUO_4$ based on reaction (2) and (3), respectively, because it is more stable by 1.9 to 9.6 kJ mol^{-1} per primitive cell than all other cases considered in the calculations. Note that, even if the ferromagnetic state of $CrUO_4$/$FeUO_4$ would be the ground state at zero temperature, other magnetic configurations at finite temperatures can still be accessible.

The DFT + *U* calculations were also used to probe the energetic stability of U^{5+} in $FeUO_4$, in comparison with other available oxidation states. In DFT + *U* calculations, manipulations of the initial magnetic moments and effective *U* parameters can be used to coax the calculation to converge in different charge states[47] (detailed methods are in ESI†). Using such approaches it was possible for $FeUO_4$ to converge to a configuration with an electronic structure consistent with the presence of U^{6+} and Fe^{2+} in $FeUO_4$, as shown in Fig. 7a. In this figure, the pDOS for the U states are consistent with a U^{6+} oxidation state, as it is characterized by the absence of a large peak corresponding to unpaired electronic states with dominant 5f electron character below the Fermi level. Further, there is a large peak of spin-down 3d valence electrons in the pDOS of Fe, which is absent in the corresponding plot for $FeUO_4$ shown in Fig. 6e; this peak reflects a larger number of occupied Fe 3d states, consistent with an Fe^{2+} oxidation state.

From the relaxed energies of the two different $FeUO_4$ electronic states (corresponding to U^{6+}/Fe^{2+} *versus* U^{5+}/Fe^{3+}), it is possible to estimate the energy for the electronic charge-transfer reaction:

$$Fe^{3+} + U^{5+} \rightarrow Fe^{2+} + U^{6+}. \quad (5)$$

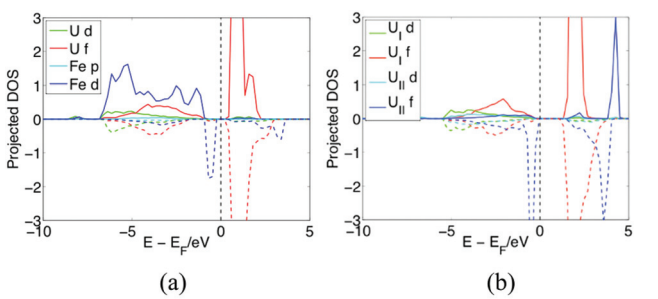

Fig. 7 Calculated pDOS for $FeUO_4$ with different oxidation states for the Fe and U cations. (a): pDOS for a pair of U^{6+} + Fe^{2+} in $FeUO_4$; (b): pDOS for a pair of U cations (U_I and U_{II}) that can be considered as U^{6+} and U^{4+} in $FeUO_4$, respectively.

The energy of the compound with the Fe^{2+}–U^{6+} pair is calculated to be 143.8 kJ mol^{-1} higher than that with Fe^{3+}–U^{5+} pair, suggesting that reaction (5) is highly unfavorable energetically. This observation is qualitatively consistent with an estimate that can be derived by combining the enthalpies of the oxidation–reduction reaction of $Fe^{3+} \rightarrow Fe^{2+}$ (147.3 kJ mol^{-1}),[13] and $U^{5+} \rightarrow U^{6+}$ (−67.8 kJ mol^{-1})[13] at room temperature, yielding 79.5 kJ mol^{-1} for reaction (5). The large endothermic enthalpy associated with reaction (5) can be understood from the Lewis acid–base interaction.[48] U^{6+} has higher acidity than U^{5+}, yet Fe^{2+} is more basic than Fe^{3+}, thus Fe^{2+}–U^{6+} pair forms an acid–base reaction that Fe^{2+} as a Lewis base may tend to donate an electron to its Lewis acid U^{6+}.

Another possible electronic configuration for $FeUO_4$ could results from the interchange of valence electrons between two U cations:

$$2\ U^{5+} \rightarrow U^{4+} + U^{6+}. \quad (6)$$

For $FeUO_4$ it was possible to converge to such an electronic configuration, and the corresponding pDOS of U cations are shown in Fig. 7b. The pDOS of one U cation (labeled as U_I in Fig. 7b) is characteristic of a U^{6+}, while the pDOS of the other U cation (labeled as U_{II} in Fig. 7b) shows a large spin-down peak from f valence electron just below Fermi level, and its absolute magnitude is much higher that the spin-up peak from f valence electron in U^{5+} in Fig. 6c and e, indicating that it is qualitatively consistent with a U^{4+} state. The energy of reaction (6) estimated from the energy difference of the $FeUO_4$ compound with U^{6+}–U^{4+} *versus* two U^{5+} cations, pair is 134.1 kJ mol^{-1}, which is again large and endothermic.

It should be noted that the calculated energies for reactions (5) and (6) reported here depend sensitively on the values of the Hubbard-*U* parameter used in the GGA + *U* computations. For $FeUO_4$, we believe the reported energies are reasonable, as the value for the Hubbard-*U* parameter used for this compound for Fe and U have been shown in previous work (see Methods section) to yield reasonable energies for redox reactions involving Fe^{2+}, Fe^{3+}, U^{4+}, U^{5+} and U^{6+} oxidation states. We are unaware of similar benchmarks having been undertaken for GGA + *U* calculations involving Cr^{2+} oxidation states, so results similar to those reported for $FeUO_4$ are not reported here for $CrUO_4$. Overall, however, the computational results presented in this section suggest that at least for the perfect stoichiometric $FeUO_4$ compounds, all uranium ions would be expected to adopt a 5+ oxidation state.

Trends of thermodynamic stability of U^{5+} and U^{6+} uranates

The enthalpies of formation from oxides for $MgUO_4$, $CrUO_4$ and $FeUO_4$ were compared with those of alkaline earth metal uranates, MUO_4 (M = Mg, Ca, Sr, and Ba), reported previously (Table 3). An approximately negative linear trend is observed (Fig. 8) between $\Delta H_{f,ox}$ and the ionic radius *r* of metal cation: $\Delta H_{f,ox} = (138.8 \pm 18.1) - (263.5 \pm 21.0)r$ kJ mol^{-1}, $R^2 = 0.9692$. Note the ionic radii of Mg^{2+}, Cr^{3+} and Fe^{3+} were obtained by subtracting that of O^{2-} from the refined bond lengths of Mg–

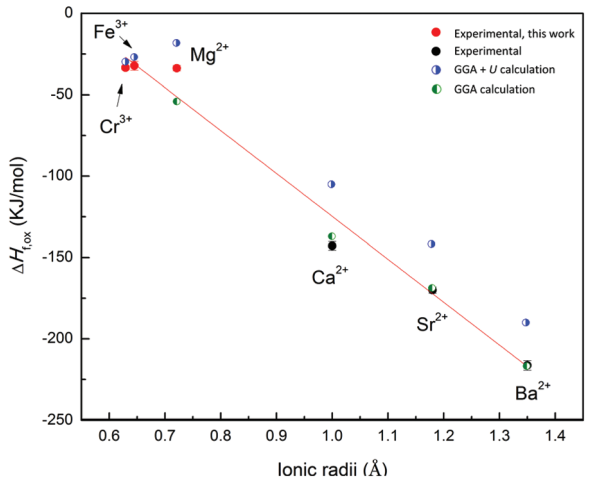

Fig. 8 Enthalpies of formation of MUO_4 from oxides (M = Ba, Sr, Ca, Mg, Cr, and Fe). Red circles, representing data points from this work; and black circles are experimental determined values. Blue and green circles represent enthalpies data from GGA + *U* and GGA calculation, respectively.

O, Cr–O and Fe–O, respectively (Table 2). Although $CrUO_4$ and $FeUO_4$ have a somewhat different structure (Cr and Fe are trivalent and U is pentavalent) from those of alkaline earth metal uranates, their $\Delta H_{f,ox}$ values follow the linear trend in Fig. 8. More specifically, $\Delta H_{f,ox}$ becomes more exothermic with increasing ionic radii of the metal cations. The general trend of increasing energetic stability with decreasing ionic potential (z/r; z is the formal charge of the metal cation, and r is its ionic radius) or decreasing oxide basicity reflects the dominance of acid–base chemistry in phase stability,[49] and has been observed in many systems including alkaline and alkaline earth cation bearing phases.[4,47,50–57]

To elaborate further, we start by noting that in the divalent-metal-containing MUO_4 compounds, all of the structures feature two U(VI)–O bonds that are shorter than the others.[23,36–38] These bonds are found in the DFT calculations to display pronounced covalent character (*c.f.*, the results presented above for $MgUO_4$ demonstrating strong hybridization between O p and U d and f states), and they can be thought of as being analogous to those found in the uranyl ion. Further, we consider the U(VI) uranates containing the divalent cations that are the strongest and weakest Lewis acids in the series, namely, $MgUO_4$ and $BaUO_4$. For $MgUO_4$, the relatively strong Lewis acid Mg^{2+} cation competes with U(VI) for the electron density on the "yl" oxygen and results in a U(VI)–O bond length that is longer than the U(VI)–O bond length in $BaUO_4$.[23,38] This suggests that the U(VI) cation is able to share more of the "yl" oxygen ion's electron density in $BaUO_4$ compared to $MgUO_4$, thereby maximizing the covalent character of the U(VI)–O bond. An examination of the GGA + *U* calculated electronic densities of states of these two uranate systems shows greater hybridization between O p and U d and f states near the Fermi level for $BaUO_4$ compared to $MgUO_4$, which is consistent with an increased covalent character of U(VI)–O bond in the former. The above analysis suggests that as the Lewis acid character of the divalent cation decreases (*i.e.*, $Ba^{2+} < Sr^{2+} < Ca^{2+} < Mg^{2+}$), there is less competition for the electron charge on the "yl" oxygen ion that forms a highly covalent bond with the neighboring U^{6+} ion. Thus, the covalent character of this bond increases as the M^{2+} cation becomes more basic, correlating with the trends towards higher energetic stability in Fig. 8.

In Fig. 8, calculated formation enthalpies have been plotted from both GGA and GGA + *U* methods (in the latter the Hubbard-*U* correction is made for the U 5f states). It is interesting to note that although both sets of results reproduce well the trends in the experimental formation enthalpies, the GGA values show better overall agreement with the absolute magnitude of the measured values for all of the divalent U(VI) uranates. In light of the discussion above, this is likely due to the importance of the hybridization in the U(VI)–O bonds in determining the energetic stability of the compounds. The introduction of the Hubbard-*U* correction is expected to lead to a higher degree of localization of the U 5f electrons, and thus a lower degree of covalency with neighboring oxygen ions relative to GGA. For this class of U(VI) containing compounds, it appears that GGA provides a more accurate description of the thermodynamic stability.

Finally, we end by noting that the observation that $\Delta H_{f,ox}$ for $CrUO_4$ and $FeUO_4$ follows the same general trend as the U(VI) containing MUO_4 compounds in Fig. 8. This suggests that the thermodynamic penalty for incorporating a trivalent metal cation coupled with reduction of U^{6+} to U^{5+} in MUO_4 is relatively small. This conclusion will be useful for predicting thermodynamic properties of other U^{5+}/U^{6+}-containing multi-component uranium phases that might be encountered in current and next generation nuclear reactors, in spent nuclear fuel, in nuclear waste, and in the transport of uranium in the environment.

Experimental methods

Sample synthesis

Both $MgUO_4$ and $CrUO_4$ can be prepared *via* calcination of mixed raw materials in air.[8] However, to achieve better homogeneity, we used co-precipitation methods that enable mixing the components at the molecular level to synthesize $MgUO_4$ and $CrUO_4$. Stoichiometric ratios of uranyl acetate ($UO_2(CH_3COO)_2{\cdot}2H_2O$) and Mg acetate ($Mg(CH_3COO)_2$) or Cr acetate ($C_8H_{16}Cr_2O_{10}$) were mixed in deionized water in a Teflon beaker. The solution was warmed at 80 °C with constant magnetic stirring. Then ammonium hydroxide was added until the solution pH reached 9 to form precipitated precursors. The mixture was then transferred to a platinum crucible and heated from 150 °C to 500 °C for about 8 hours for complete drying. The retrieved powder was ground, mixed again, and calcined under O_2 at 1200 °C ($MgUO_4$) or 1450 °C ($CrUO_4$) for 24 hours.

However, $FeUO_4$ synthesis was unsuccessful by regular solid state synthesis, coprecipitation, or hydrothermal methods.[1]

Thus we chose a sealed tube method because of its proven success, though the specific synthesis procedure was modified to produce more homogeneous $FeUO_4$. A stoichiometric mixture of dried U_3O_8 and Fe_3O_4 was produced by hand grinding the starting materials in a mortar for half an hour. This mixture was pressed into a ~50 mg pellet, contained in a small covered Pt crucible and then sealed in a silica tube under vacuum. The loaded silica tube was then heated at 950 °C for 7 days, followed by another heating cycle at 975 °C for 7 days. Intermediate grinding was done to improve homogeneity.

Chemical and structural analyses

XRD patterns were collected for each synthesis product by grinding 5 mg of the sample into a fine powder with ethanol and depositing the paste onto a zero-background quartz slide. Diffraction patterns were collected from 16 to 83° in 2θ with a step size of 0.011° and a collection time of 2 s per step using a Bruker D8 Advance diffractometer equipped with CuK_α radiation and a solid-state detector. A single phase product was identified for all the three samples. Lattice parameters were determined using the Rietveld method[58] with the GSAS program.[59] Chemical compositions and sample homogeneity were checked with EPMA using a Cameca SX50 coupled with wavelength dispersive spectrometry (WDS), at an accelerating voltage of 20 keV, a probe current of 10 nA and a spot size of 1 μm. Quantitative WDS was conducted using a lower accelerating voltage of 15 keV. UO_2, MgO, Cr_2O_3, and Fe_2O_3 were used as analytical standards for U, Mg, Cr and Fe, respectively.

The oxidation state of U was determined by XANES spectroscopy at the GSECARS X-ray microprobe beamline (13-ID-E) at the Advanced Photon Source (APS), Argonne National Laboratory (Argonne, IL USA). XANES spectra were collected in transmission mode using a 200 mm long, helium filled ion chamber to monitor incident flux, I_0 (ADC IC-400-200) and a 50 mm long nitrogen filled ion chamber downstream of the sample to monitor transmitted flux, I_1 (ADC 500-50). XANES spectra were obtained by scanning a Si(111) monochromator through the U L_{III} absorption edge (~17 166 eV) and recording the total absorption. In the XANES region the energy step sizes were 2.5 eV from 17 066 to 17 146 eV and 0.25 eV from 17 146 to 17 191 eV. The EXAFS portion of the spectra was then collected to a distance of 15 $Å^{-1}$. Dwell time at each energy step was 1 s, and up to eight spectra were collected and summed to improve signal-to-noise ratios. Energy calibration was obtained using a Y metal foil (first derivative peak defined to be 17 037 eV). The samples were prepared as thin powder layers mounted between Scotch tapes. The X-ray absorption spectroscopy data processing software Athena[60] was used for analysis, and software Artemis[60] was used for EXAFS fitting.

XPS were performed using a Kratos Axis DLD spectrometer equipped with a monochromatic X-ray source of Al K_α source (15 mA, 14 keV). The instrument work function was calibrated to give a binding energy (BE) of 83.96 ± 0.05 eV for the Au $4f_{7/2}$ line for metallic gold and the spectrometer dispersion was adjusted to give a BE of 932.62 ± 0.05 eV for the Cu $2p_{3/2}$ line of metallic copper. High resolution analyses were carried out with an analysis area of 300 × 700 microns and a pass energy of 80 eV. The Kratos charge neutralizer system was used on all specimens. Spectra have been charge corrected to the main line of the carbon 1s spectrum (adventitious carbon) which was set to 285.0 eV. Spectra were analyzed using CasaXPS software (version 2.3.16 PR 1.6).

Mössbauer spectra were collected using a 50-mCi (initial strength) $^{57}Co/Rh$ source. The velocity transducer MVT-1000 (WissEL) was operated in a constant acceleration mode (23 Hz, ±5 or 12 mm s^{-1}). An Ar–Kr proportional counter was used to detect the radiation transmitted through the holder, and the counts were stored in a multichannel scalar (MCS) as a function of energy (transducer velocity) using a 1024 channel analyzer. Data were folded to 512 channels to give a flat background and a zero-velocity position corresponding to the CS of a metal iron foil at RT. Calibration spectra were obtained with a 25 μm-thick α-Fe(m) foil (Amersham, England) placed in the same position as the samples to minimize errors due to geometry changes. A closed-cycle cryostat (ARS, Allentown, PA) was employed for below RT measurements. Sample preparation is similar to the previously reported procedures.[61]

Theoretical methods

DFT calculations were performed with the Vienna ab initio simulation package (VASP),[31,33] within the projector augmented wave (PAW) formalism.[30,35] For the exchange correlation functional we employed the generalized gradient approximation (GGA) as parameterized by Perdew, Burke, and Ernzerhof (PBE).[32] For the PAW potentials, U ($6s^2$, $6p^6$, $5f^3$, $6d^1$, $7s^2$), Fe ($3p^6$, $3d^7$, $4s^1$), Cr ($3p^6$, $3d^5$, $4s^1$), Mg ($2s^2$, $2p^6$, $3s^2$), Ca ($3s^2$, $3p^6$, $4s^2$), Sr ($4s^2$, $4p^6$, $5s^2$), Ba ($5s^2$, $5p^6$, $6s^2$), and O ($2s^2$, $2p^4$) electrons were treated as valence states, while the remaining electrons were frozen as core states. The cut-off energy for the plane wave basis was 520 eV, and the convergence criterion for the electron-density self-consistency cycles was 10^{-6} eV. For sampling of the Brillouin zone we employed the Monkhorst–Pack scheme,[62] with (5 × 2 × 5) *k*-point grids for the $Cr_4U_4O_{16}$ and $Fe_4U_4O_{16}$ primitive supercells, (5 × 5 × 5) *k*-point grids for $Mg_4U_4O_{16}$, $Sr_4U_4O_{16}$ and $Ba_4U_4O_{16}$ primitive supercells, and an (8 × 8 × 8) *k*-point grid for the $CaUO_4$ primitive supercell used in the calculations. The *k*-point grids for simple oxides have equal or higher densities in the reciprocal space compared with those for uranate supercells.

The DFT + *U* formalism by Dudarev *et al.* was used to account for the strong on-site Coulomb repulsion for the localized Fe/Cr 3d states and U 5f states.[34] In the implementation of the GGA + *U* formalism, the choices for the effective Hubbard *U* parameters (*i.e.*, *U–J*, hereafter referred to simply as *U*) were chosen as follows. For iron we used *U* = 4.3 eV, a value that has been widely used in the literature for studies of reactions involving charge transfer between Fe^{3+} and Fe^{2+} cations. An example of such an application is the electrochemical reaction for battery cathode materials: $LiFePO_4 \rightarrow Li^+ + e^- + FePO_4$.[63] Values of *U* in the range of 4.0 to 4.3 eV for Fe have also been found to yield results comparing well with experiments and higher levels of theory for bulk hematite

(Fe_2O_3).[64–66] For Cr we used U = 3.7 eV, a value recommended by Materials Project website[67] to reproduce the redox reaction energy between Cr_2O_3 and CrO_3 as $2Cr_2O_3 + 3O_2 \rightarrow 4CrO_3$. A similar value of U = 3.5 eV for Cr was also widely used for the calculations of oxidation reactions of transition metals with O_2.[68,69] For U we used U = 4.0 eV, which was found to provide good agreement between calculated and measured oxidation enthalpies of UO_2 and energetic stabilities of rare earth doped UO_2.[70,71]

Calorimetry

High temperature oxide melt solution calorimetry[72,73] was conducted using a custom built Tian-Calvet twin microcalorimeter.[72,73] Powdered samples were hand pressed into small pellets (~7 mg) and were dropped from room temperature into ~20 g of molten sodium molybdate ($3Na_2O{\cdot}4MoO_3$) at 702 °C or 802 °C or ~30 g of molten lead borate ($2PbO{\cdot}B_2O_3$) at 802 °C inside a Pt crucible. Dissolution of uranium oxides and their drop solution enthalpy data in both solvents at different calorimetric conditions were conducted and obtained previously[5,46,74,75] and this work. The calorimeter was calibrated against the heat contents of ~5 mg α-Al_2O_3 pellets.[72,73] O_2 gas was continuously bubbled through the melt at 5 ml min^{-1} to ensure an oxidizing environment and to facilitate dissolution of samples.[76] Flushing O_2 gas with ~50 ml min^{-1} through the calorimeter chamber assisted in maintaining a constant gas environment above the solvent.[76] Upon rapid and complete dissolution of the sample, the enthalpy of drop solution, ΔH_{ds}, was obtained. Finally, using an appropriate thermochemical cycle (Tables S3–S5 in ESI†), the enthalpies of formation from the oxides, $\Delta H_{f,ox}$, and from the elements, ΔH_f°, at room temperature were calculated.

Acknowledgements

This study, including synthesis, characterization, DFT calculations and calorimetric measurements, was supported as part of the Materials Science of Actinides, an Energy Frontier Research Center, funded by the U.S. Department of Energy, Office of Science, Office of Basic Energy Sciences under Award Number DESC0001089. The Mossbauer and XPS analyses were performed using EMSL, a DOE Office of Science User Facility sponsored by the Office of Biological and Environmental Research and located at Pacific Northwest National Laboratory. PNNL is operated by Battelle for the U.S. DOE under contract DE-AC06-76RLO1930. The XAS work was performed at GeoSoilEnviroCARS (Sector 13), Advanced Photon Source (APS), Argonne National Laboratory. GeoSoilEnviroCARS is supported by the National Science Foundation – Earth Sciences (EAR-1128799) and Department of Energy – GeoSciences (DE-FG02-94ER14466). Use of the Advanced Photon Source was supported by the U. S. Department of Energy, Office of Science, Office of Basic Energy Sciences, under Contract No. DE-AC02-06CH11357. The last stage of this work was also supported by the laboratory-directed research and development (LDRD) program, through the G. T. Seaborg Institute, of Los Alamos National Laboratory (LANL), which is operated by Los Alamos National Security LLC, under DOE Contract DE-AC52-06NA25396, in that X.G. is now pursuing a Seaborg postdoctoral fellowship at LANL.

Notes and references

1 H. R. Hoekstra and R. H. Marshall, *Adv. Chem. Ser.*, 1967, 211.
2 P. A. G. Ohare, J. Boerio and H. R. Hoekstra, *J. Chem. Thermodyn.*, 1976, **8**, 845–855.
3 J. Selbin and J. D. Ortego, *Chem. Rev.*, 1969, **69**, 657.
4 *Thermodynamics of uranium minerals and related materials*, ed. A. Navrotsky, T. Shvareva and X. Guo, Mineralogical Association of Canada, 2013, ch. 4, pp. 147–164.
5 X. Guo, A. Navrotsky, R. K. Kukkadapu, M. Engelhard, A. Lanzirotti, M. Newville, S. R. Sutton and H. Xu, *Geochim. Cosmochim. Acta*, 2015, under review.
6 K. A. Kraus and F. Nelson, *J. Am. Chem. Soc.*, 1949, **71**, 2517–2522.
7 D. Cohen, *J. Inorg. Nucl. Chem.*, 1970, **32**, 3525.
8 E. J. Felten, E. F. Juenke and S. F. Bartram, *J. Inorg. Nucl. Chem.*, 1962, **24**, 839–845.
9 M. Greenbla, R. Hornreic and B. Sharon, *J. Solid State Chem.*, 1974, **10**, 371–376.
10 P. A. G. Ohare, J. Boerio, D. R. Fredrickson and H. R. Hoekstra, *J. Chem. Thermodyn.*, 1977, **9**, 963–972.
11 G. C. Allen, A. J. Griffiths and B. J. Lee, *Transition Met. Chem.*, 1978, **3**, 229–233.
12 G. C. Allen, A. J. Griffiths and C. W. Suckling, *Chem. Phys. Lett.*, 1978, **53**, 309–312.
13 R. A. Robie and B. S. Hemingway, *Thermodynamic properties of minerals and related substances at 298.15 K and 1 bar pressure and at higher temperatures*, 1995.
14 F. Chen, R. C. Ewing and S. B. Clark, *Am. Mineral.*, 1999, **84**, 1208.
15 E. H. P. Cordfunke, A. S. Booij and M. E. Huntelaar, *J. Chem. Thermodyn.*, 1999, **31**, 1337–1345.
16 D. Labroche, J. Rogez, J. P. Laval and O. Dugne, *Schr. Fz. Jul. Energ.*, 2000, **15**, 89–92.
17 d. B. S. Van, M. Verwerft, J. P. Laval, B. Gaudreau, P. G. Allen and W. A. Van, *J. Solid State Chem.*, 2002, **166**, 320–329.
18 K.-A. Kubatko, K. Helean, A. Navrotsky and P. C. Burns, *Am. Mineral.*, 2006, **91**, 658–666.
19 A. V. Soldatov, D. Lamoen, M. J. Konstantinovic, d. B. S. Van, A. C. Scheinost and M. Verwerft, *J. Solid State Chem.*, 2007, **180**, 54–61.
20 J. H. Liu, d. B. S. Van and M. J. Konstantinovic, *J. Solid State Chem.*, 2009, **182**, 1105–1108.
21 E. S. Ilton and P. S. Bagus, *Surf. Interface Anal.*, 2011, **43**, 1549–1560.
22 R. M. Haag and C. R. Muncy, *J. Am. Ceram. Soc.*, 1964, **47**, 34–36.

23 W. H. Zachariasen, *Acta Crystallogr.*, 1954, **7**, 788–791.
24 D. Jakes and I. Krivy, *J. Inorg. Nucl. Chem.*, 1974, **36**, 3885–3885.
25 H. J. Borchardt, *J. Inorg. Nucl. Chem.*, 1959, **12**, 113–121.
26 D. K. Smith, C. F. Cline and D. E. Sands, *Nature*, 1961, **192**, 861–862.
27 M. Bacmann, E. F. Bertaut and G. Bassi, *Bull. Soc. Fr. Mineral. Cristallogr.*, 1965, **88**, 214.
28 M. Bacmann and E. F. Bertaut, *Bull. Soc. Fr. Mineral. Cristallogr.*, 1967, **90**, 257.
29 M. Bacmann, E. F. Bertaut, A. Blaise, R. Chevalie and G. Roult, *J. Appl. Phys.*, 1969, **40**, 1131.
30 P. Blöchl, *Phys. Rev. B: Condens. Matter*, 1994, **50**, 17953–17979.
31 G. Kresse and J. Furthmuller, *Comput. Mater. Sci.*, 1996, **6**, 15–50.
32 J. Perdew, K. Burke and M. Ernzerhof, *Phys. Rev. Lett.*, 1996, **77**, 3865–3868.
33 G. Kresse and J. Furthmuller, *Phys. Rev. B: Condens. Matter*, 1996, **54**, 11169–11186.
34 S. Dudarev, G. Botton, S. Savrasov, C. Humphreys and A. Sutton, *Phys. Rev. B: Condens. Matter*, 1998, **57**, 1505–1509.
35 G. Kresse and D. Joubert, *Phys. Rev. B: Condens. Matter*, 1999, **59**, 1758–1775.
36 W. H. Zachariasen, *Acta Crystallogr.*, 1948, **1**, 281–285.
37 E. A. Ippolitova, I. P. Simanov, L. M. Kovba, G. P. Polunina and I. A. Bereznikova, *Radiokhimiya*, 1959, **1**, 660–664.
38 S. Samson and S. G. Sillen, *Ark. Kemi, Mineral. Geol.*, 1947, A25.
39 Y. Yun, J. Rusz, M. T. Suzuki and P. M. Oppeneer, *Phys. Rev. B: Condens. Matter*, 2011, 83.
40 S. D. Kelly, K. M. Kemner, J. Carley, C. Criddle, P. M. Jardine, T. L. Marsh, D. Phillips, D. Watson and W. M. Wu, *Environ. Sci. Technol.*, 2008, **42**, 1558–1564.
41 N. Belai, M. Frisch, E. S. Ilton, B. Ravel and C. L. Cahill, *Inorg. Chem.*, 2008, **47**, 10135–10140.
42 B. Kosog, H. S. La Pierre, M. A. Denecke, F. W. Heinemann and K. Meyert, *Inorg. Chem.*, 2012, **51**, 7940–7944.
43 E. Murad and J. Cashion, *Mössbauer spectroscopy of environmental materials and their industrial utilization*, Kluwer Academic Publications, Norwell, Massachusetts, 2004, pp. 418.
44 I. Grenthe, J. Fuger, R. J. M. Konings, R. J. Lemire, A. B. Muller, C. Nguyen-Trung and H. Wanner, *Chemical Thermodynamics of Uranium*, Elsevier, Amsterdam, 1992.
45 J. M. McHale and A. Navrotsky, *Chem. Mater.*, 1997, **9**, 1538–1546.
46 X. Guo, S. Szenknect, A. Mesbah, S. Labs, N. Clavier, C. Poinssot, S. V. Ushakov, H. Curtius, D. Bosbach, R. C. Ewing, P. C. Burns, N. Dacheux and A. Navrotsky, *Proc. Natl. Acad. Sci. U. S. A.*, 2015, **112**, 6551–6555.
47 X. Guo, A. H. Tavakoli, S. Sutton, R. K. Kukkadapu, L. Qi, A. Lanzirotti, M. Newville, M. Asta and A. Navrotsky, *Chem. Mater.*, 2014, **26**, 1133–1143.
48 D. W. Smith, *J. Chem. Educ.*, 1987, **64**, 480–481.
49 A. Navrotsky, *Am. Mineral.*, 1994, **79**, 589–605.
50 H. W. Xu, A. Navrotsky, M. D. Nyman and T. M. Nenoff, *J. Mater. Res.*, 2000, **15**, 815–823.
51 H. W. Xu, A. Navrotsky, M. Nyman and T. M. Nenoff, *Microporous Mesoporous Mater.*, 2004, **72**, 209–218.
52 H. W. Xu, A. Navrotsky, Y. L. Su and M. L. Balmer, *Chem. Mater.*, 2005, **17**, 1880–1886.
53 H. W. Xu, A. Navrotsky, M. L. Balmer and Y. Su, *Phys. Chem. Miner.*, 2005, **32**, 426–435.
54 X. Guo, Z. Rak, A. H. Tavakoli, U. Becker, R. C. Ewing and A. Navrotsky, *J. Mater. Chem. A*, 2014, **2**, 16945–16954.
55 J. Q. Qi, X. F. Guo, A. Mielewczyk-Gryn and A. Navrotsky, *J. Solid State Chem.*, 2015, **227**, 150–154.
56 X. Guo, R. K. Kukkadapu, A. Lanzirotti, M. Newville, M. H. Engelhard, S. R. Sutton and A. Navrotsky, *Inorg. Chem.*, 2015, **54**, 4156–4166.
57 H. Xu, L. Wu, J. Zhu and A. Navrotsky, *J. Nucl. Mater.*, 2015, **459**, 70–76.
58 H. M. Rietveld, *J. Appl. Crystallogr.*, 1969, **2**, 65.
59 A. C. Larson and R. B. Von Dreele, Los Alamos National Laboratory Report LAUR, 2000, 84–748.
60 B. Ravel and M. Newville, *J. Synchrotron Radiat.*, 2005, **12**, 537–541.
61 T. S. Peretyazhko, J. M. Zachara, R. K. Kukkadapu, S. M. Heald, I. V. Kutnyakov, C. T. Resch, B. W. Arey, C. M. Wang, L. Kovarik, J. L. Phillips and D. A. Moore, *Geochim. Cosmochim. Acta*, 2012, **92**, 48–66.
62 H. J. Monkhorst and J. D. Pack, *Phys. Rev. B: Solid State*, 1976, **13**, 5188–5192.
63 F. Zhou, T. Maxisch and G. Ceder, *Phys. Rev. Lett.*, 2006, **97**, 155704.
64 N. J. Mosey, P. Liao and E. A. Carter, *J. Chem. Phys.*, 2008, **129**, 014103.
65 Z. D. Pozun and G. Henkelman, *J. Chem. Phys.*, 2011, **134**, 224706.
66 G. Rollmann, P. Entel, A. Rohrbach and J. Hafner, *Phase Trans.*, 2005, **78**, 251–258.
67 https://materialsproject.org/.
68 A. Jain, G. Hautier, S. P. Ong, J. P. Moore, C. C. Fischer, K. A. Persson and G. Ceder, *Phys. Rev. B: Condens. Matter*, 2011, **84**, 045115.
69 L. Wang, T. Maxisch and G. Ceder, *Phys. Rev. B: Condens. Matter*, 2006, **73**, 195107.
70 J. M. Solomon, V. Alexandrov, B. Sadigh, A. Navrotsky and M. Asta, *Acta Mater.*, 2014, **78**, 282–289.
71 B. E. Hanken, C. R. Stanek, N. Grønbech-Jensen and M. Asta, *Phys. Rev. B: Condens. Matter*, 2011, **84**, 085131.
72 A. Navrotsky, *Phys. Chem. Miner.*, 1977, **2**, 89–104.
73 A. Navrotsky, *Phys. Chem. Miner.*, 1997, **24**, 222–241.
74 K. B. Helean, A. Navrotsky, E. R. Vance, M. L. Carter, B. Ebbinghaus, O. Krikorian, J. Lian, L. M. Wang and J. G. Catalano, *J. Nucl. Mater.*, 2002, **303**, 226–239.
75 X. Guo, S. V. Ushakov, S. Labs, H. Curtius, D. Bosbach and A. Navrotsky, *Proc. Natl. Acad. Sci. U. S. A.*, 2014, **111**, 17737–17742.
76 A. Navrotsky, R. P. Rapp, E. Smelik, P. Burnley, S. Circone, L. Chai and K. Bose, *Am. Mineral.*, 1994, **79**, 1099–1109.